Supporting Information

Sequential catalysis controls selectivity in electrochemical CO_2 reduction on Cu

Yanwei Lum and Joel W. Ager*

Joint Center for Artificial Photosynthesis and Materials Science Division, Lawrence Berkeley National Laboratory, California 94720, United States

Department of Materials Science and Engineering, University of California, Berkeley, California 94720, United States

*jwager@lbl.gov

Table of Contents

Experimental

Materials

Cesium carbonate (99.995% metals basis), potassium phosphate monobasic (99.99% metals basis), potassium phosphate dibasic (99.95% metals basis), nitric acid (70%) and sulfuric acid (99.999% metals basis) were purchased from Sigma-Aldrich. Copper sputtering target (99.999%), silver sputtering target (99.99%), carbon sputtering target (99.999%), gold pellets (99.99%) and titanium pellets (99.999%) were purchased from Kurt J. Lesker Company. Silicon wafers were purchased from University Wafer, Inc. Silicon wafers with 1 µm thick thermal oxide layer (SiO_2) were purchased from Silicon Valley Microelectronics, Inc. Selemion AMV anionic exchange membranes were purchased from Asahi Glass Co., Ltd. Acetone and isopropanol were purchased from BDH. Photolithography was carried out using positive photoresist (Shipley Microposit S1818) and development of the photoresist was performed using MF-26A developer. The MF-26A developer was purchased from Dow Electronic Materials and contains TMAH (tetramethylammonium hydroxide). All chemicals were used without further purification. Photolithography masks (made of chrome/quartz) were purchased from Photo Sciences, Inc. Conductive copper tape was purchased from 3M. Carbon dioxide (99.995%), nitrogen (99.999%), argon (99.999%) and hydrogen (99.999%) were purchased from Praxair. Hydrogen, argon, nitrogen and carbon dioxide gas purifiers purchased from Valco Instruments Co. Inc were used on the gas feeds to the electrochemical cell and gas chromatograph. 18.2 MΩ deionized (DI) water was produced by a Millipore system.

Fabrication of interdigitated AuCu devices

Silicon wafers with 1 µm thick thermal oxide layer (SiO_2 substrates) were broken into semi-rectangular pieces of at least 2.5 cm by 2.5 cm, with one such piece sufficient to fabricate a single AuCu device (see Figure S5 for optical image). This piece was first spin-coated with S1818 positive photoresist and subsequently soft-baked for 90 seconds on a hot plate heated to a temperature of 100 °C. Patterning was then carried out with a photolithography mask with the appropriate design and an aligner equipped with an UV lamp. The exposed photoresist was then developed in MFA-26A developer for 60 seconds, rinsed copiously with DI water and then dried with a stream of nitrogen. Next, 4 nm of Ti (adhesion layer) followed by 100 nm of Au was deposited using e-beam evaporation (Angstrom NEXDEP 006). Lift-off was then carried out by sonicating in acetone, followed by rinsing in isopropanol. The two sets of lines were ensured to be electronically insulated from each other (non-shorting) by connecting a multimeter to the top and bottom contact and checking the resistance. Devices were only deemed to be successfully fabricated if there was no reading on the multimeter even after contact was made. Separate pieces of copper tape were then pasted onto the top and bottom contact for ease of electrical connection (Figure S5). Cu was then subsequently deposited on only one set of lines by electrodeposition using a custom-made compression type electrochemical cell with an o-ring to limit the electrodeposition area to 1.767 cm^2 (Figure S5). The Cu deposition solution used was 500 mM $CuSO_4$ solution adjusted to pH 1 with H_2SO_4. The working electrode lead on the potentiostat was connected to the set of lines where copper deposition is desired and the counter electode lead was connected to the other set of lines. It is important to use the other set of lines as the counter electrode as this significantly decreases any unwanted deposition of copper onto the surface. To fabricate the 55%, 21%, 11% and 3% AuCu device, a constant cathodic current density of 1, 0.82, 0.66 and 0.3 mA cm^{-2} respectively was applied for 8 minutes. After deposition was complete, the device was rinsed and soaked in DI water for 5 minutes and later dried with a stream of nitrogen. More information can be found in Figures S3 to S9 and Table S2.

Fabrication of lithographically patterned Cu dots/lines on Au or Ag substrates

8 nm of Ti (adhesion layer) followed by 200 nm of Au or Ag was deposited onto a Si substrate via reactive sputtering using an AJA International ATC Orion 5 sputtering system (Figure S14). The rest of the

fabrication, which involves photolithography, metal deposition and lift-off is identical to that of the AuCu device. In this case however, 30 nm of Cu was deposited onto the substrate for all samples. Samples with a carbon interlayer in between the Ag substrate and Cu were fabricated similarly, with the exception of the deposition of 30 nm of carbon via sputtering followed by the 30 nm Cu layer. More information can be found in Figures S13 to S19 and Table S4.

Electrochemical measurements

For all electrochemical measurements described in this work, a Biologic SP-300 potentiostat was used. CO_2 reduction was carried out using a custom-made electrochemical cell made of PEEK and fitted with Teflon o-rings for chemical inertness and durability.[1] In this cell, the working and counter electrodes are both constrained to be 1 cm^2 and sit parallel to each other to ensure a uniform potential distribution across the working electrode surface. To ensure that the electrolyte remains saturated with CO_2 throughout electrolysis, CO_2 gas was continuously introduced into the electrochemical cell at a rate of 5 sccm (using a mass-flow controller). A custom-made glass frit fabricated by Adams & Chittenden Scientific Glass was used to disperse the gas into the electrolyte as well as provide adequate convection in the electrochemical cell. Before carrying out CO_2 reduction experiments, CO_2 gas was allowed to flow through the electrolyte in the cathode chamber for at least 15 minutes to ensure that the electrolyte is saturated with CO_2. To separate the electrolyte in the cathode and anode chambers, a Selemion AMV anion exchange membrane was employed. Before use, the membrane was carefully rinsed with DI water and completely dried with a stream of N_2. The electrolyte volume used in both the cathode and anode were 1.8 ml each. Before use in experiments, the electrochemical cell was sonicated in 20 wt.% nitric acid for 1 hour. All bulk electrolysis CO_2 reduction experiments were conducted for 70 minutes. A leak-free Ag/AgCl electrode from Innovative Instruments, Inc was employed as a reference electrode. The accuracy of this reference electrode was ensured periodically by comparison with a custom-made reversible hydrogen electrode. To convert potentials vs Ag/AgCl to the RHE scale, the following equation as used:

$$\mathrm{E\ (vs.RHE)} = \mathrm{E\ (vs.Ag/AgCl)} + 0.197\ \mathrm{V} + 0.0591\ \mathrm{pH},$$

where the pH was 6.8 for 0.1 M $KHCO_3$. After saturation of the electrolyte with CO_2, the solution resistance was determined using potentiostatic electrochemical impedance spectroscopy (PEIS), scanning through a frequency range of 1 MHz to 10 Hz. 85% of the solution resistance was then compensated using the software and the remaining 15% was post-corrected after the experiment.

Product analysis

All gas product analysis (hydrogen, methane, carbon monoxide and ethylene) described in this work were performed using a MG#3 Gas Chromatograph from SRI Instruments, equipped with a 12" long HaySep D column and argon as the carrier gas. The electrochemical cell was linked directly to the gas chromatograph to enable continuous online analysis of the gas products. Detection of the hydrogen was achieved using a TCD detector and detection of the hydrocarbons was achieved using a FID equipped with a methanizer. The gas chromatograph was calibrated using calibration tanks containing varying amounts of hydrogen, carbon monoxide, methane, ethylene and ethane. CO_2 reduction experiments were carried out for 70 minutes and analysis of the gas products was done at the 10, 25, 40, 55 and 70 min marks. The average of these values was taken to give the reported data.

The liquid products were collected from the cathode and anode chambers after electrolysis and analyzed by High-Performance Liquid Chromatography (HPLC) on UltiMate 3000 from Thermo Scientific. Vials with the collected samples were placed in an autosampler holder and 10 μL of sample was injected into the column. The column used was an Aminex HPX 87-H (Bio-Rad) and diluted sulfuric acid (1 mM) was used as the eluent. The temperature of the column was maintained at 60 °C in a column oven, and the separated compounds were detected with a refractive index detector (RID). Calibrations were performed using dilute solutions of the expected products of the CO_2 reduction reaction (CO_2R): glyoxal, glycolaldehyde, formate, formaldehyde, acetate, ethylene glycol, hydroxyacetone, acetaldehyde, methanol, allyl alcohol, ethanol, propionaldehyde and n-propanol. Catalysis measurements were typically carried out 3 times with fresh electrolyte and electrodes; data reported are an average of these measurements. Faradaic efficiency and current density data for Cu foil as reported in Figures 4 to 8 were taken from data reported previously.[1]

Preparation of electrolytes

0.1 M $CsHCO_3$ was prepared by bubbling of CO_2 through 0.05 M Cs_2CO_3 for 1 hour. The pH was checked at the end of the bubbling to ensure that a pH of 6.8 was attained.

CO transport and pH modeling

More information regarding CO transport and surface pH modeling is available in the simulation details section.

Simulation details

Modeling schematic of AuCu interdigitated device

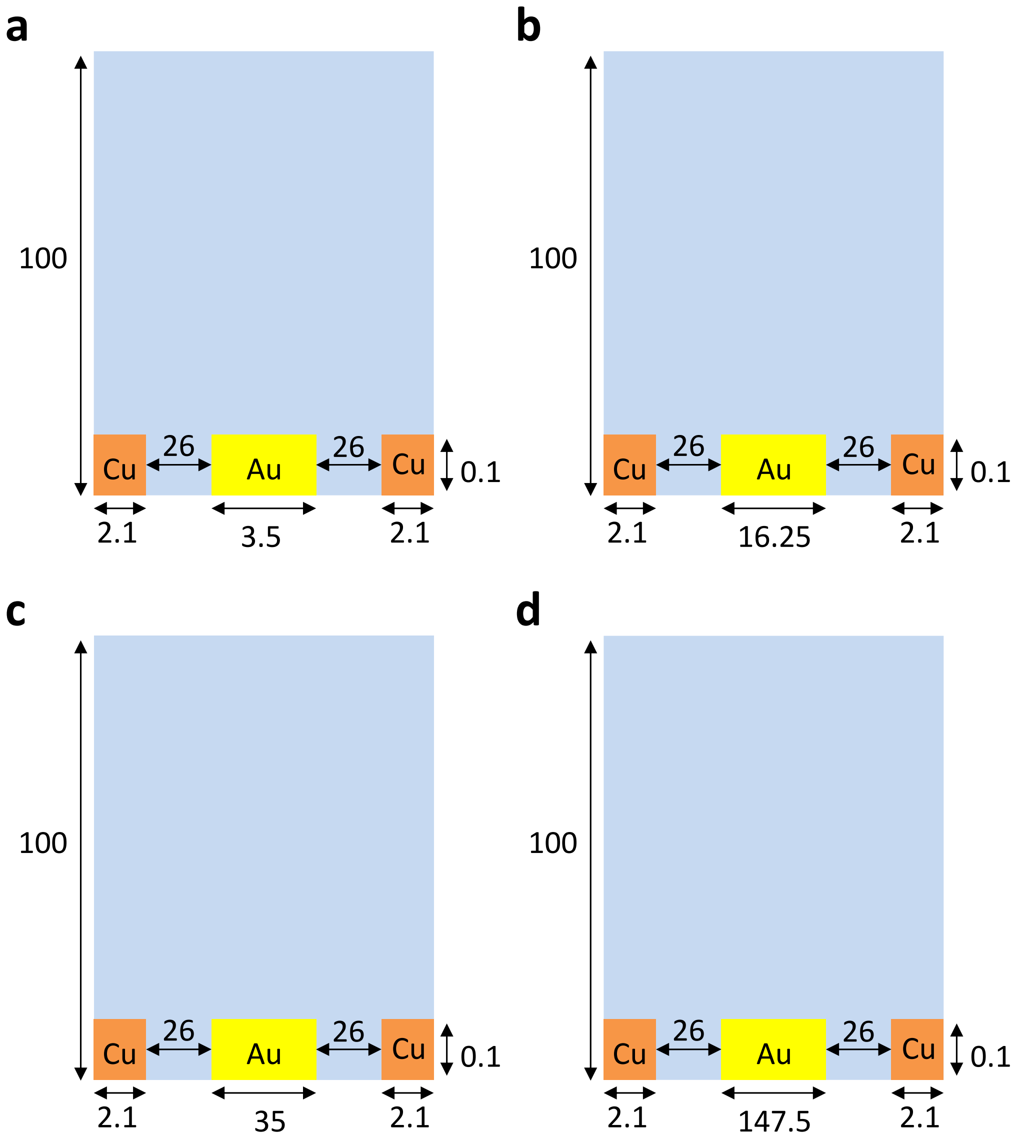

*drawings not to scale, all units in µm

Figure S1: Modeling schematic of the AuCu interdigitated device system. The AuCu device consists of two sets of lines, the Cu lines which have a width of 4.2 µm and the Au lines which can have widths of 3.5, 16.25, 35 and 147.5 µm, depending on the desired configuration.

Modeling of CO transport

2D diffusion transport modeling was implemented in COMSOL Multiphysics 5.1 to solve the equations:

$$\frac{\partial C}{\partial t} + \nabla.(-D\nabla C) = R \qquad (1)$$

$$N = -D\nabla C \qquad (2)$$

where *C* is the concentration of CO, *D* is diffusion coefficient of CO, *R* is the rate of production of CO and *N* is the CO flux. Table S1 shows a list of modeling parameters with their associated values.

Table S1: Modeling parameters with their associated values

Parameter	Value
Boundary layer thickness	100 μm
Initial concentration of CO in bulk electrolyte	Zero
Diffusion coefficient of CO	2.03×10^{-9} m^2 s^{-1}
CO flux from Au	1.6×10^{-8} mol cm^{-2} s^{-1} / 3.0 mA cm^{-2}
CO concentration on Cu	Zero (ideal sink)

Varying sink ideality for AuCu device

For the modeling discussed in the main portion of the paper, the CO concentration on the Cu surface was set at zero (ideal sink). Under this assumption, for the 55% AuCu device, 62% of the CO which is generated on the Au undergoes further conversion on the Cu. Here, the effect on sink non-ideality (i.e. values less than 1) is modeled for the case of the 55% AuCu device and the results are plotted in Figure S2.

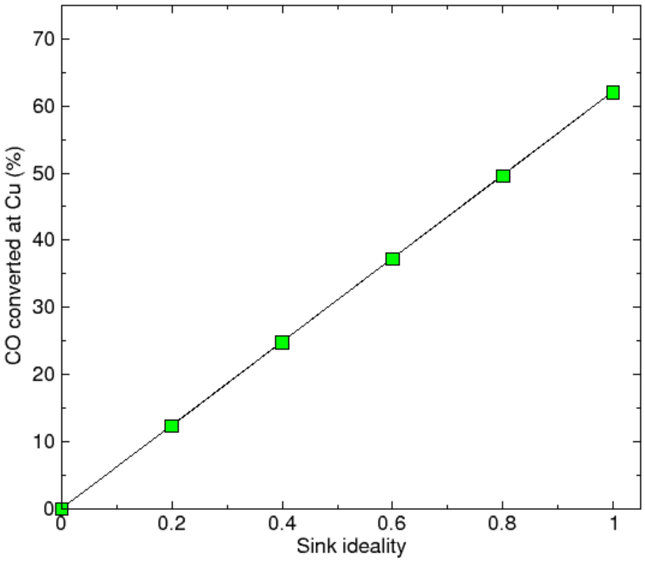

Figure S2: Effect of sink ideality on the percentage of CO consumed for the 55% AuCu device.

Fabrication and images of interdigitated devices

Design schematic of AuCu interdigitated device

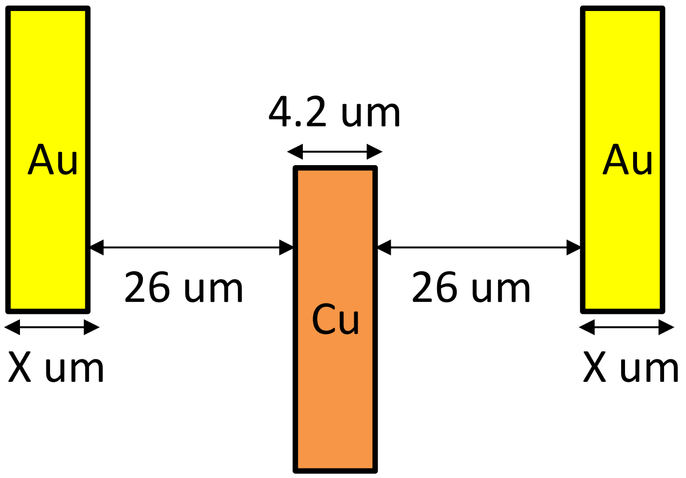

Figure S3: Design schematic of the AuCu interdigitated device system. The AuCu device consists of two sets of lines, the Cu lines which have a width of 4.2 µm and the Au lines which can have widths of 3.5, 16.25, 35 and 147.5 µm, depending on the desired configuration (see Table S2 for more information).

Table S2: Design parameters of the AuCu interdigitated device system. 4 such devices can be fabricated, each with different widths of Au lines, giving Cu compositions of 55, 21, 11 and 3%.

AuCu device	Cu composition* (%)	X (µm)	Surface coverage of Cu (%)	Surface coverage of Au (%)	Surface coverage of SiO_2 (%)
1	55	3.5	7.04	5.86	87.1
2	21	16.25	5.79	22.4	71.8
3	11	35.0	4.61	38.4	57.0
4	3	147.5	2.06	72.4	25.5

*These are calculated values based on SEM images and this gives the geometric area of Cu over total geometric area of all metal lines.

Fabrication of AuCu interdigitated devices

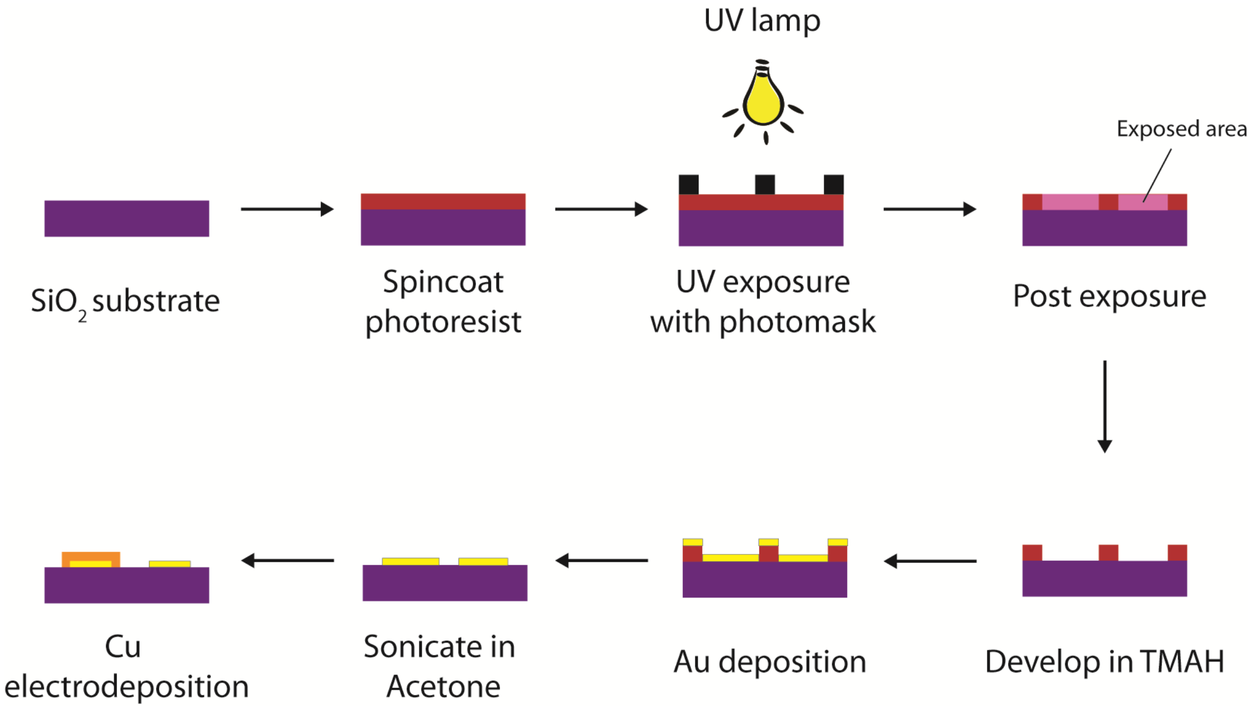

Figure S4: Fabrication schematic of the AuCu devices. Positive photoresist is spin coated onto a Si substrate with a 1 µm SiO_2 layer. The photoresist is patterned with a photomask and an aligner equipped with a UV source. The photoresist is then developed with MF-26A (contains TMAH). 4nm of Ti (adhesion layer) followed by 100 nm of Au is deposited and lift-off is subsequently achieved by sonicating in acetone. Cu is then electrodeposited on one set of the lines.

Optical images of AuCu device

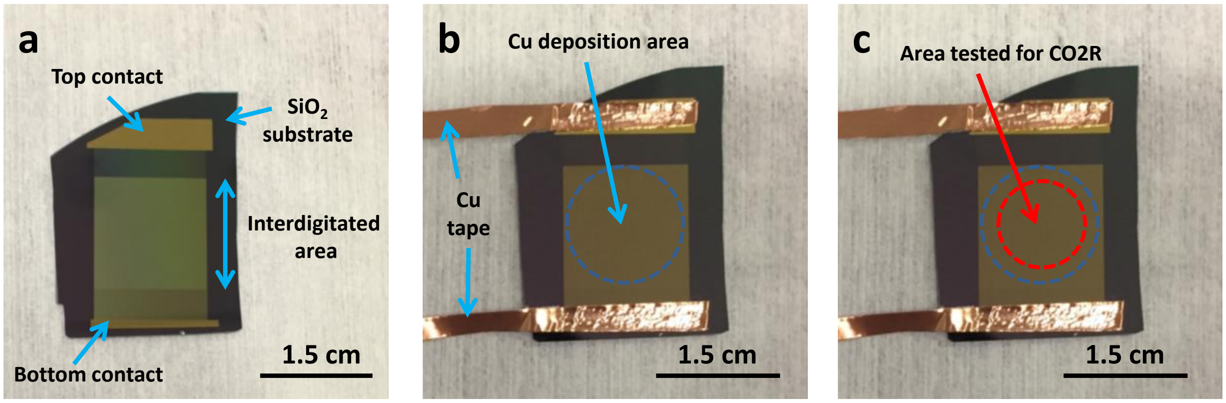

Figure S5: Optical images of: (a) 11% AuCu device after deposition of Au and lift-off with acetone. (b) Separate pieces of Cu tape have been attached to the top and bottom contacts and the device is ready for Cu electrodeposition on one set of lines. The area to be deposited with Cu is demarcated with a dashed blue circle. (c) After Cu electrodeposition on one set of lines, the device is ready for CO_2R and the tested area is demarcated with a dashed red circle.

SEM and EDX images of AuCu device (no Cu)

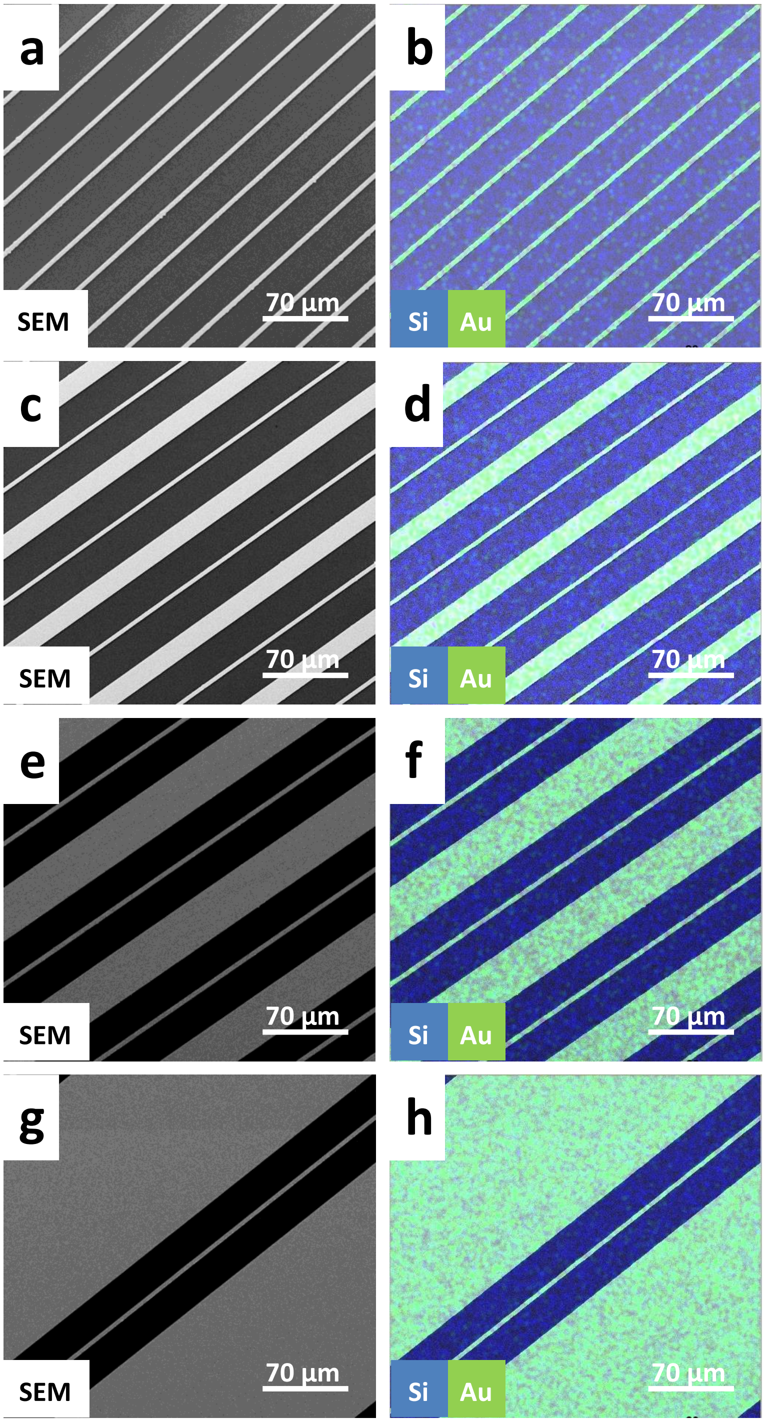

Figure S6: SEM images and corresponding EDX images of the 4 AuCu devices with no Cu deposited, (a)/(b): 55%, (c)/(d): 21%, (e)/(f): 11%, (g)/(h): 3%. Si is shown in blue and Au is shown in green.

SEM and EDX images of AuCu device (with Cu)

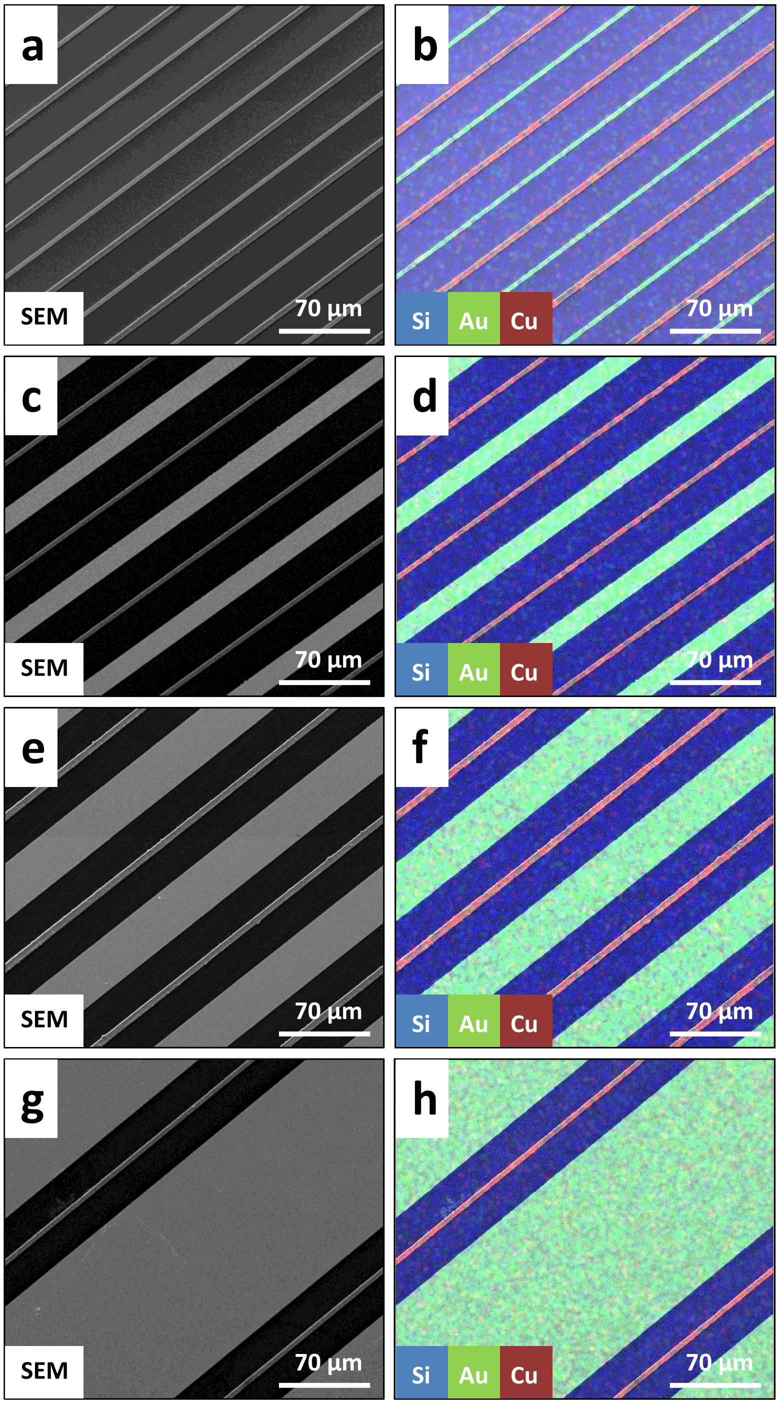

Figure S7: SEM images and corresponding EDX images of the 4 AuCu devices with Cu deposited: (a) and (b) 55%, (c) and (d) 21%, (e) and (f) 11%, (g) and (h) 3%. Si is shown in blue, Au is shown in green and Cu is shown in red.

SEM images of a Cu line and a Au line

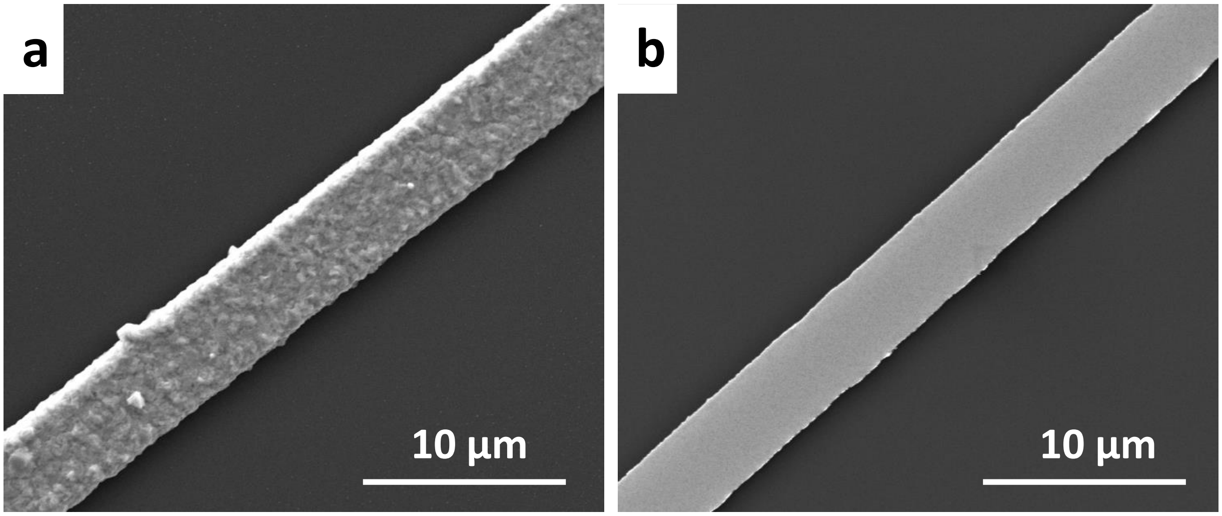

Figure S8: SEM images of: (a) line with Cu deposited onto its surface. (b) Au line with no Cu deposited onto its surface. Cu lines are made by electrodeposition onto Au lines. These images are from the 55% AuCu device.

SEM and EDX images of a Cu line at the boundary

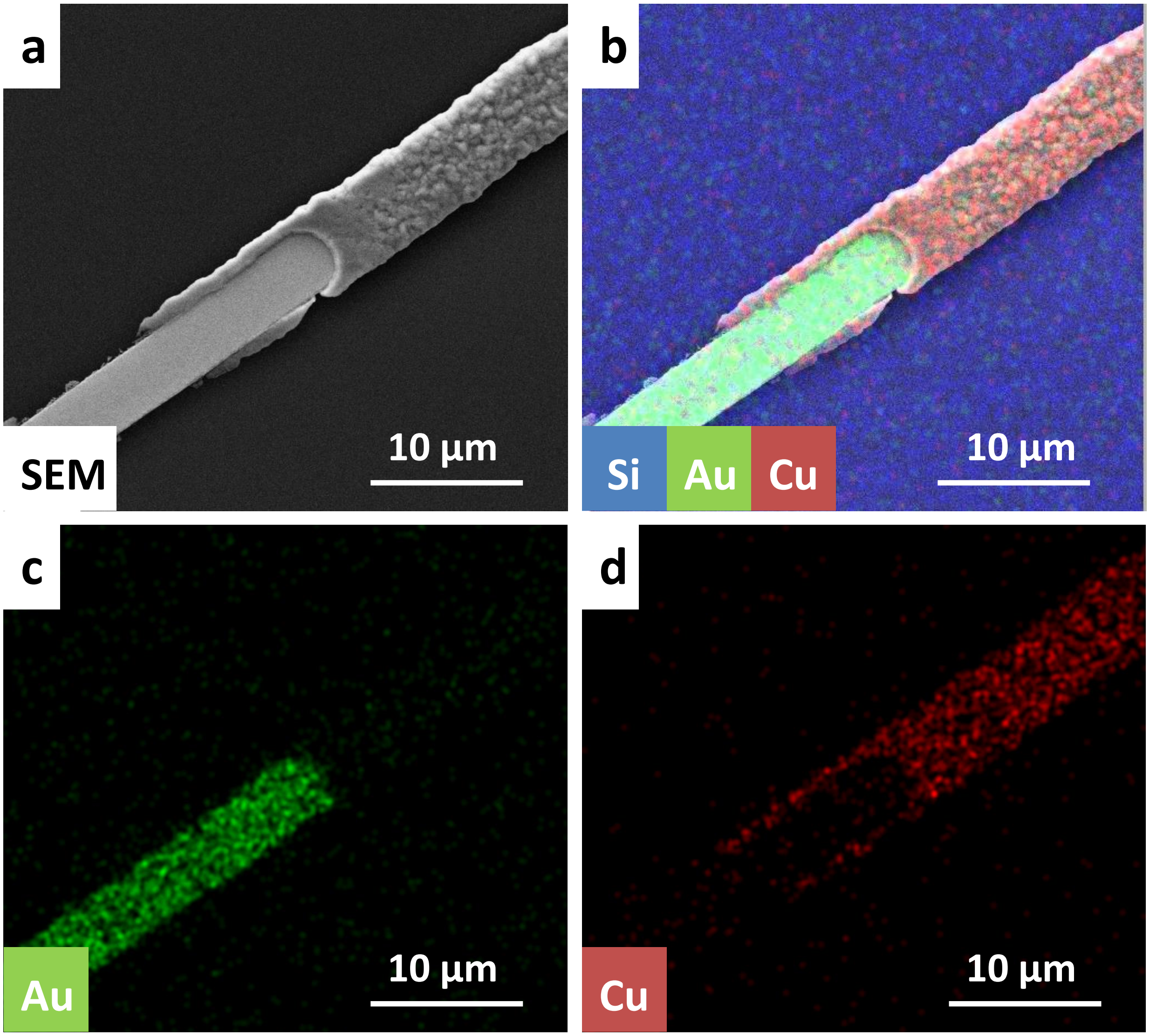

Figure S9: (a) SEM image of the boundary on a line where Cu deposition is absent (area outside the blue circle, see Figure S5b). (b) EDX image showing the elements Au (green), Si (blue) and Cu (red). (c) EDX image showing only Cu (red). (d) EDX image showing only Au (green).

Supplemental electrocatalysis data for interdigitated devices

Breakdown of oxygenates generated by AuCu devices (C_2 products)

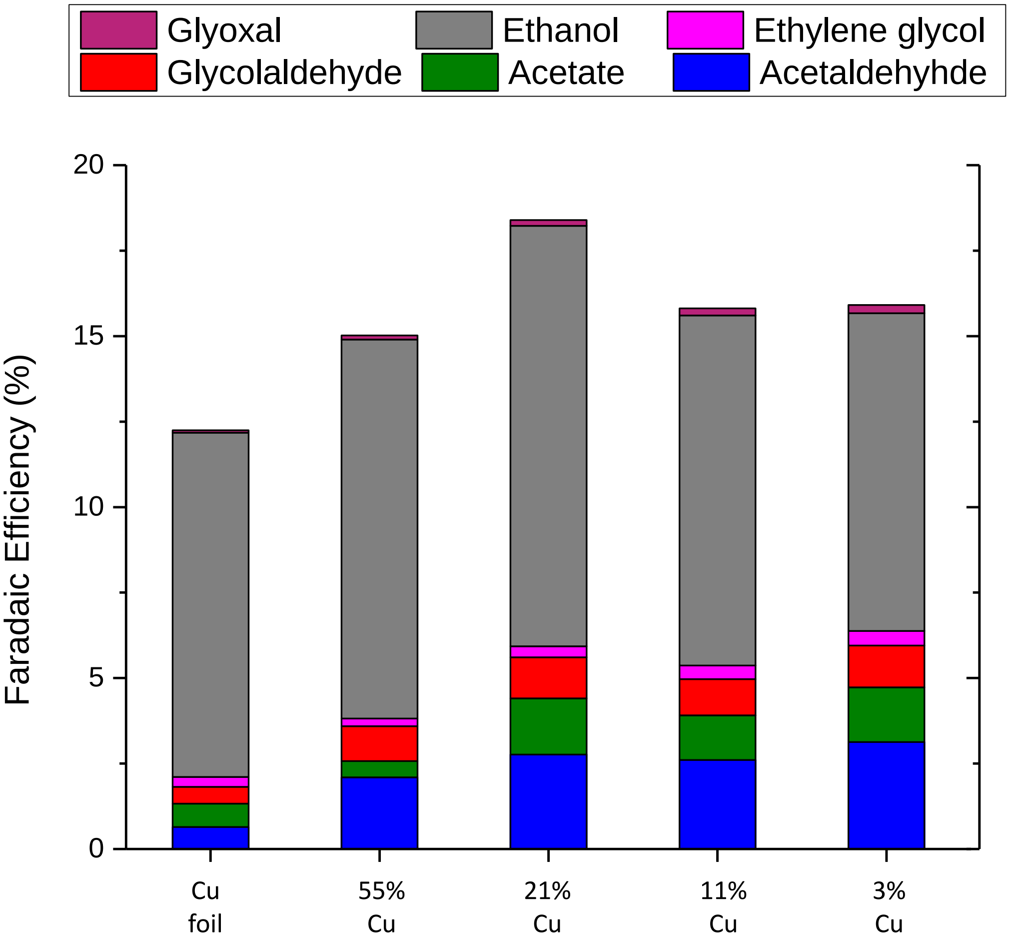

Figure S10: Faradaic efficiency to C_2 oxygenates for the AuCu devices. Data for Cu foil is shown for reference. Note the increase in acetaldehyde and acetate FE as at lower relative Cu coverages.

Breakdown of oxygenates generated by AuCu devices (C_3 products)

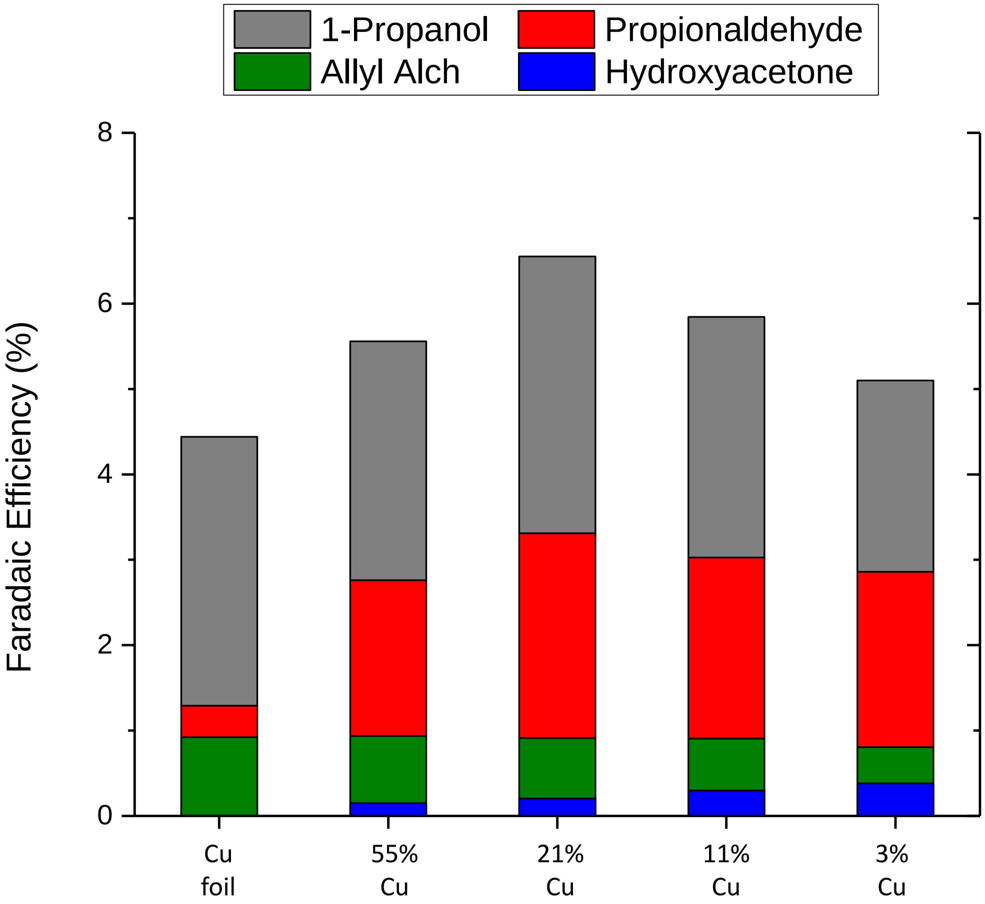

Figure S11: Faradaic efficiency to C_3 oxygenates for the AuCu devices. Data for Cu foil is shown for reference. Note the enhanced production of propionaldehyde at lower relative Cu coverages.

Calculation of fraction of total CO molecules going towards specific product

To calculate the fraction of total CO molecules going to for example, propanol, the partial current density to propanol has to be calculated first. Next, the partial current density can be converted into a molar flux by dividing by the Faraday's constant. The molar flux is then divided by 18 (number of electrons to create 1 molecule of propanol) and multiplied by 3 (number of CO required per propanol molecule) to obtain the molar rate of CO consumption to produce propanol. This calculation can be repeated for all CO derived products and the molar rate of CO consumption to produce all these products can be summed up to obtain a total molar rate of CO consumption. The fraction of total CO molecules going to propanol is the molar rate of CO consumption to produce propanol divided by the total molar rate of CO consumption. Table S3 shows an example calculation for the 55% AuCu device.

Table S3: Calculation of fraction of total CO molecules going to specific product for 55% AuCu device

Product	Partial current density (mA cm^{-2})	Number of electrons per molecule	Number of CO molecules required	Molar rate of CO consumption (mol cm^{-2} s^{-1})	Total molar rate of CO consumption to CO derived products (mol cm^{-2} s^{-1})	Fraction of total CO molecules going towards product
Methane	0.41	8	1	5.23E-10	7.17E-09	0.073
Glyoxal	0.01	6	2	3.07E-11		0.004
Acetate	0.03	8	2	8.93E-11		0.012
Glyocolaldehyde	0.08	8	2	1.96E-10		0.027
Ethylene glycol	0.02	10	2	3.45E-11		0.005
Acetaldehyde	0.15	10	2	3.21E-10		0.045
Ethanol	0.82	12	2	1.41E-09		0.196
Ethylene	2.25	12	2	3.81E-09		0.531
Hydroxyacetone	0.01	14	3	2.47E-11		0.003
Allyl alcohol	0.06	16	3	1.13E-10		0.016
Propionaldehyde	0.13	16	3	2.62E-10		0.037
Propanol	0.21	18	3	3.57E-10		0.050

Partial current density difference between Au+Cu and Cu only

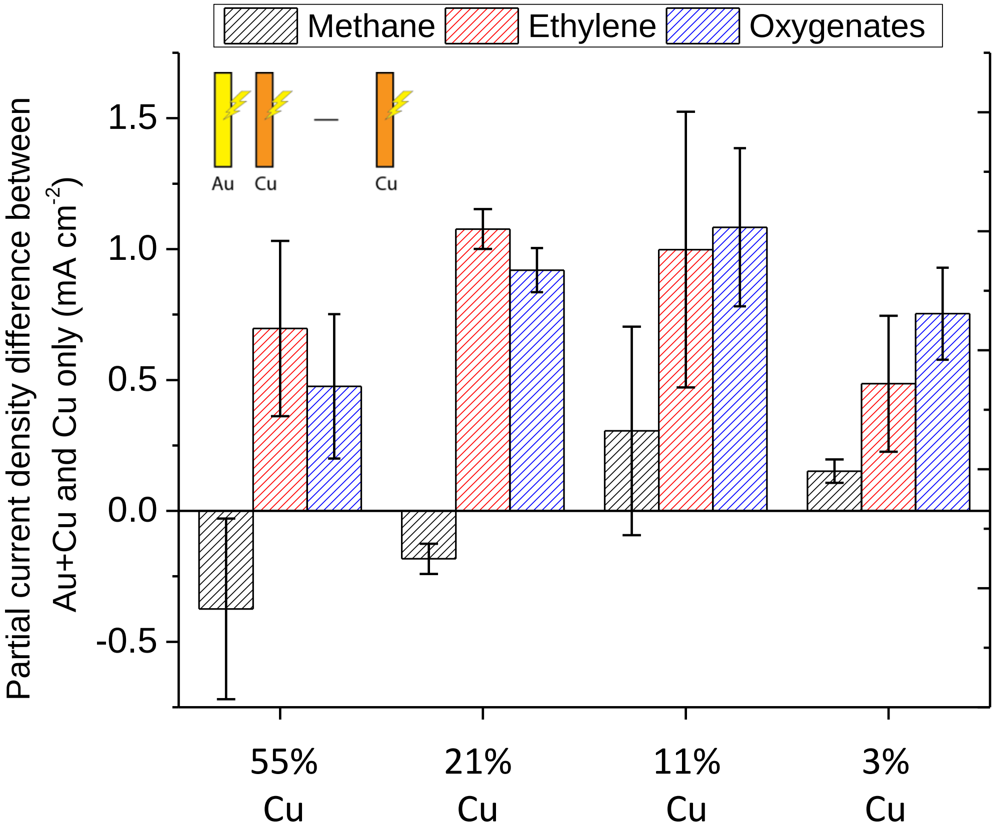

Figure S12: Partial current density difference for methane, ethylene and oxygenates when both Au and Cu are actuated compared to when only Cu is actuated.

Fabrication and images of Cu lines and dots on Ag and Au

Design schematic of Cu dots/lines on Ag system

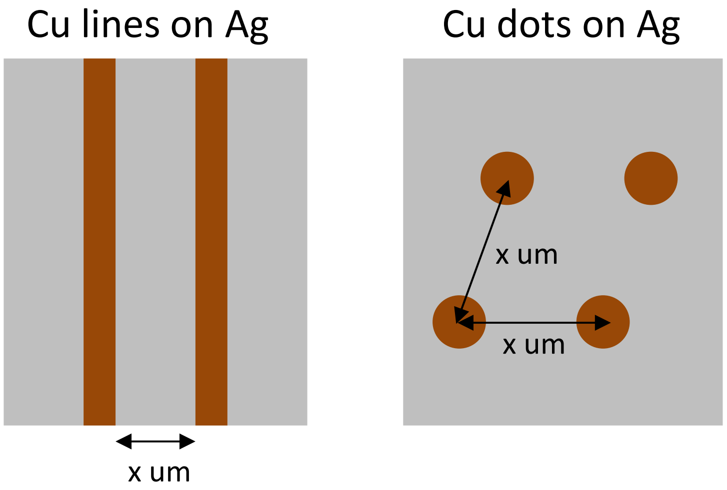

Figure S13: Design schematic of the Cu dots/lines system on a Ag substrate. The spacings between two Cu lines can be varied to achieve different areal coverages of Cu. Similarly for the Cu dots, the nearest neighbor distance between each dot determines the areal coverages of Cu (see Table S4 for more information). Lines are 8.6 µm wide and dots have a diameter of 1.6 µm.

Table S4: Design parameters of the Cu dots/lines system on a Ag substrate. 4 different designs of Cu lines and 4 different designs of Cu dots were created, each giving a different areal coverage of Cu.

Design	x (µm)	Designed Cu composition (%)	Measured Cu composition*(%)
8.6 µm Cu lines on Ag	39	18.1	18.2
	25	25.6	25.6
	8	51.8	51.8
	2.5	77.4	77.2
1.6 µm Cu dots on Ag	11.5	1.8	2.4
	7.5	4.1	4.3
	5.5	7.7	7.8
	3.5	19.0	18.8

*Measured Cu composition determined via scanning electron microscopy and image processing software.

Fabrication of Cu dots/lines on Ag system

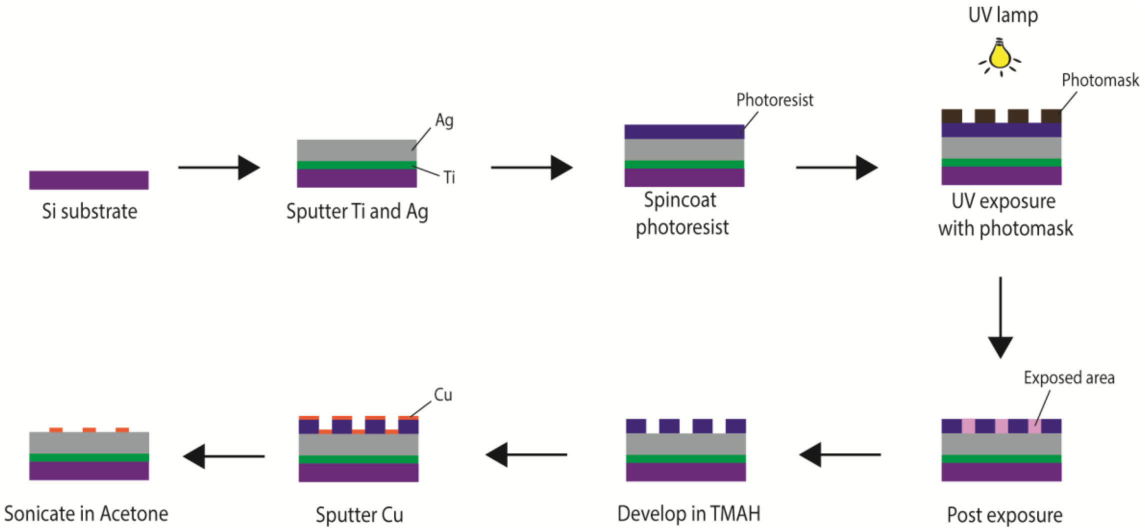

Figure S14: Fabrication schematic of the Cu dots/lines on Ag system. Ag substrates are made by sputtering 8 nm of Ti (adhesion layer) followed by 200 nm of Ag on a Si substrate. Positive photoresist is spin coated and the photoresist is patterned with a photomask and aligner equipped with a UV source. The photoresist is then developed with MF-26A (contains TMAH). 30 nm of Cu is then deposited and lift-off is subsequently achieved by sonicating in acetone.

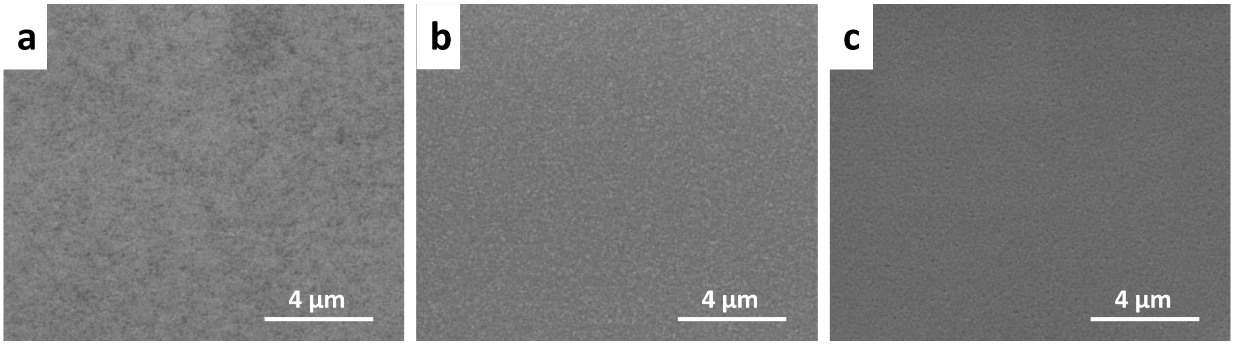

Figure S15: SEM images of: (a) Au substrate, (b) Ag substrate and (c) 30 nm of Cu blanket deposited onto a Ag substrate (100% Cu on Ag).

SEM images of 18.2% Cu lines on a Au substrate

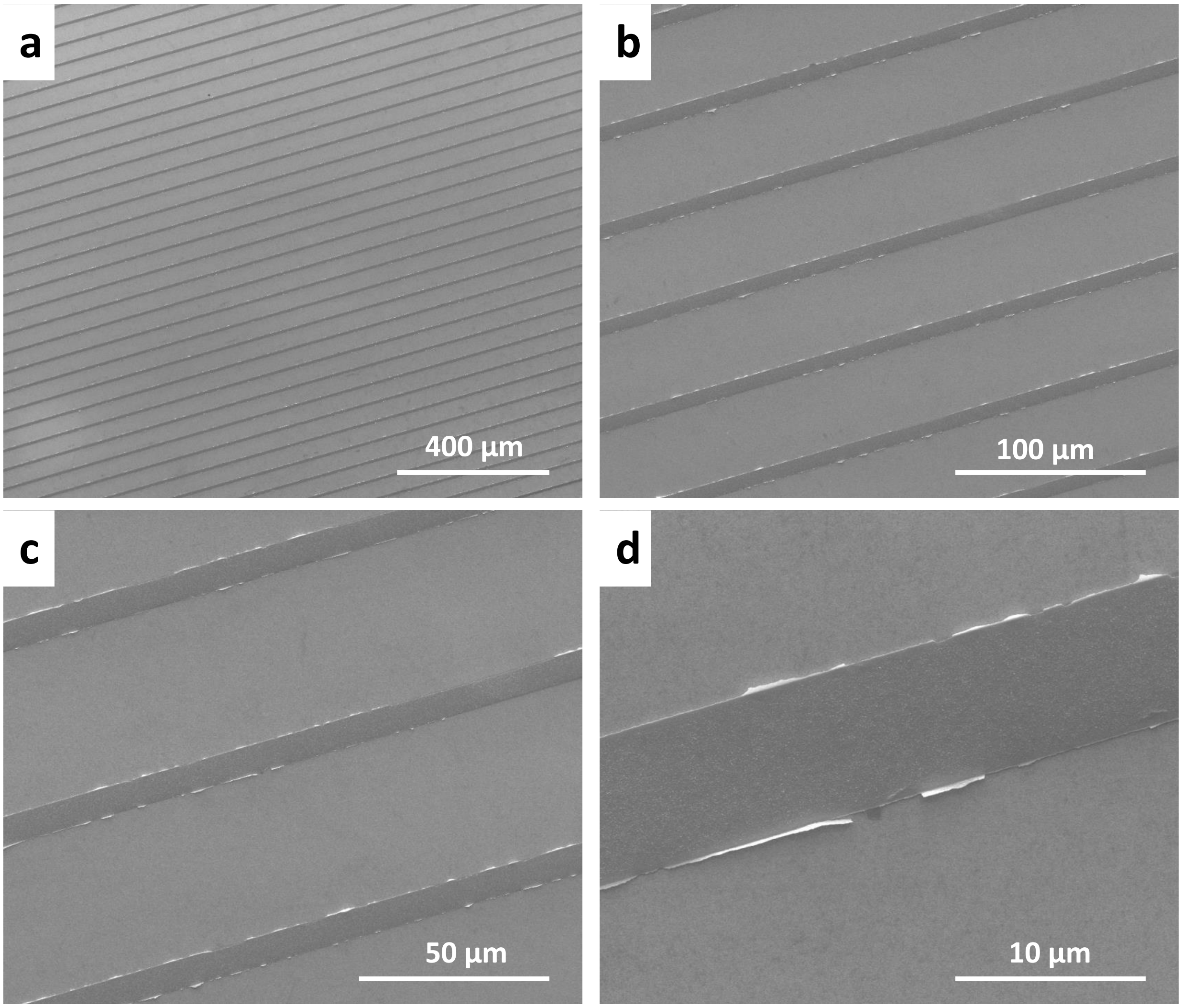

Figure S16: SEM images of 18.2% Cu lines on a Au substrate with different degrees of magnification.

SEM images of Cu lines on Ag system

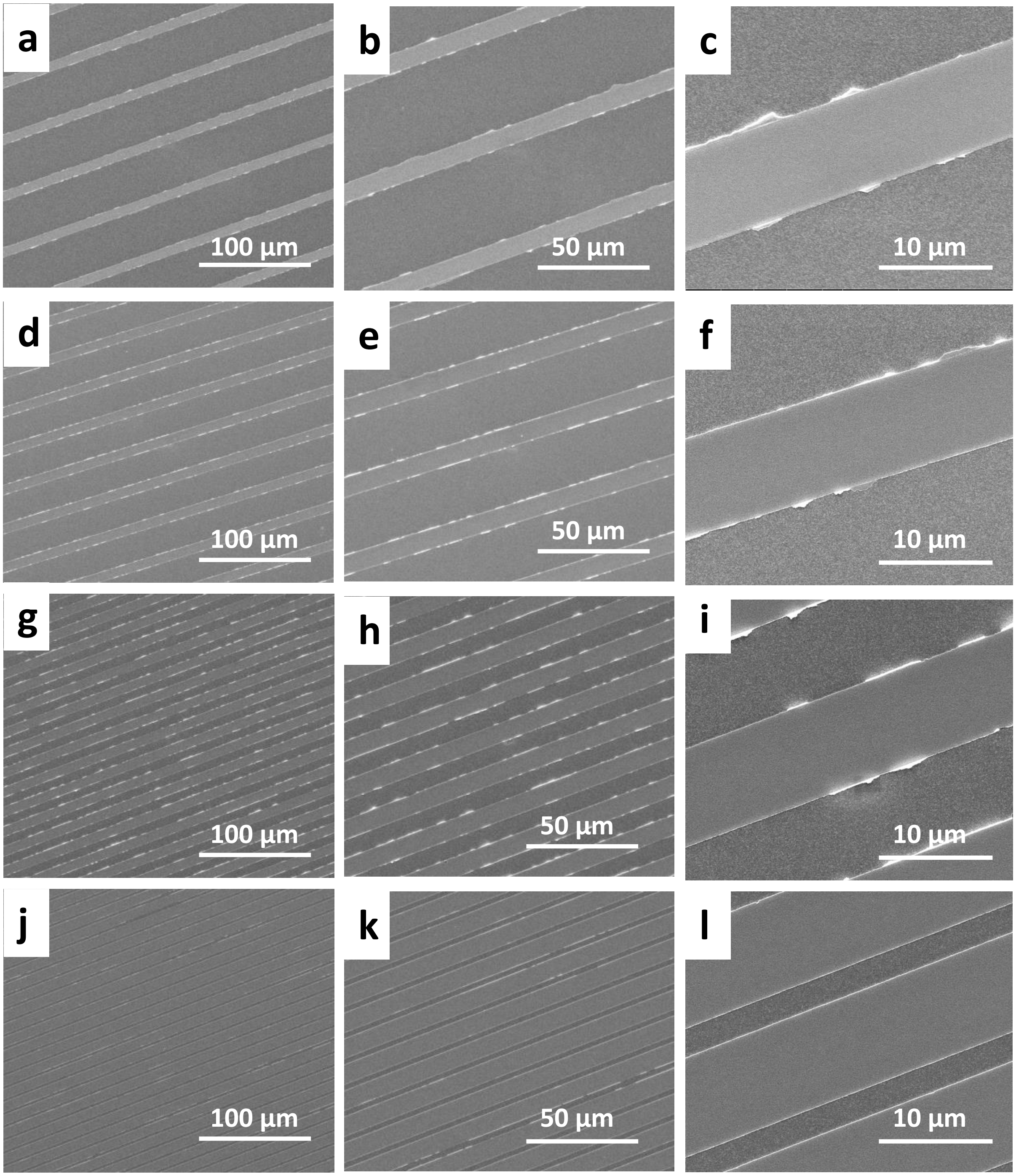

Figure S17: SEM images of (a)-(c): 18.2% Cu lines on Ag, (d)-(f): 25.6% Cu lines on Ag, (g)-(i): 51.8% Cu lines on Ag and (j)/(l): 77.2% Cu lines on Ag.

SEM images of the Cu dots on Ag system

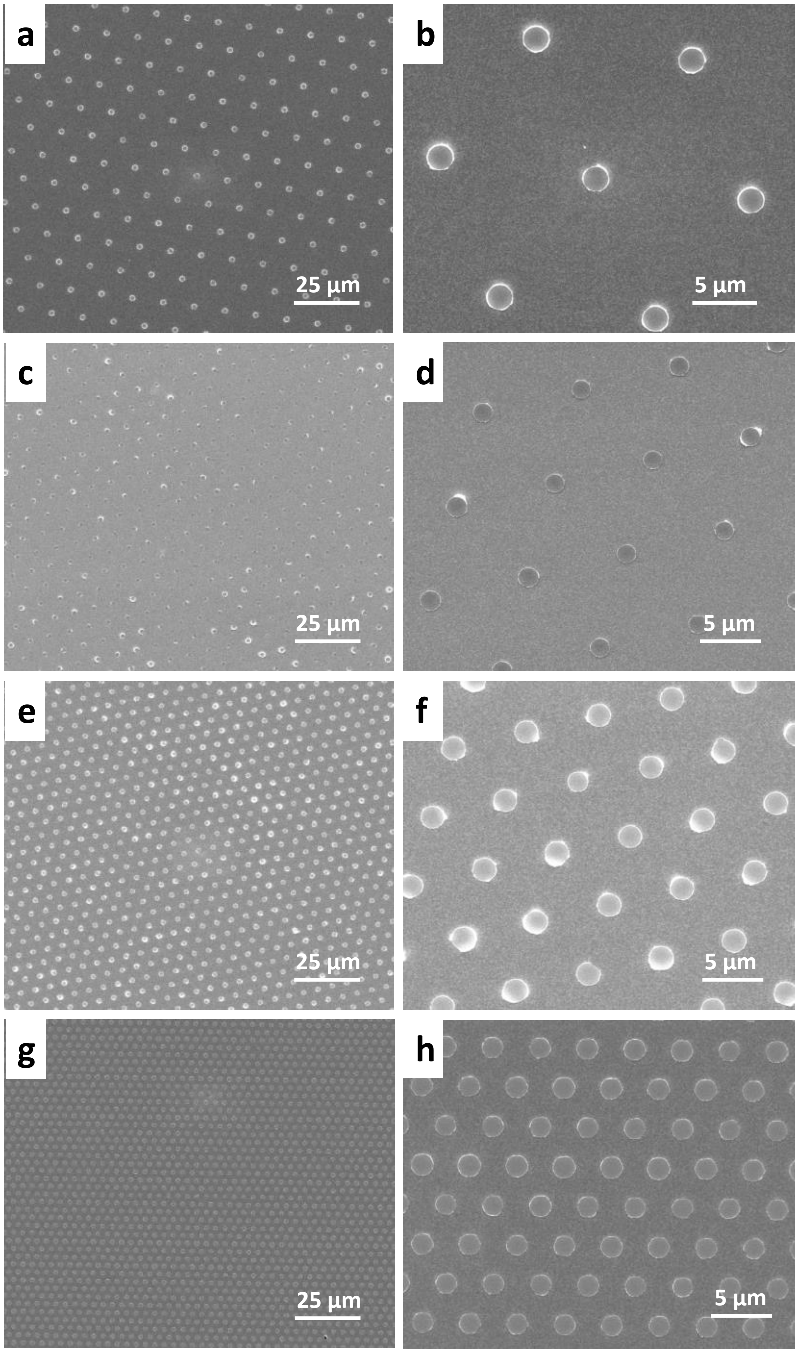

Figure S18: SEM images of (a)/(b): 2.4% Cu dots on Ag, (c)/(d): 4.3% Cu dots on Ag, (e)/(f): 7.8% Cu lines on Ag and (g)/(h): 18.8% Cu dots on Ag.

SEM images of Cu dots on Ag with carbon interlayer

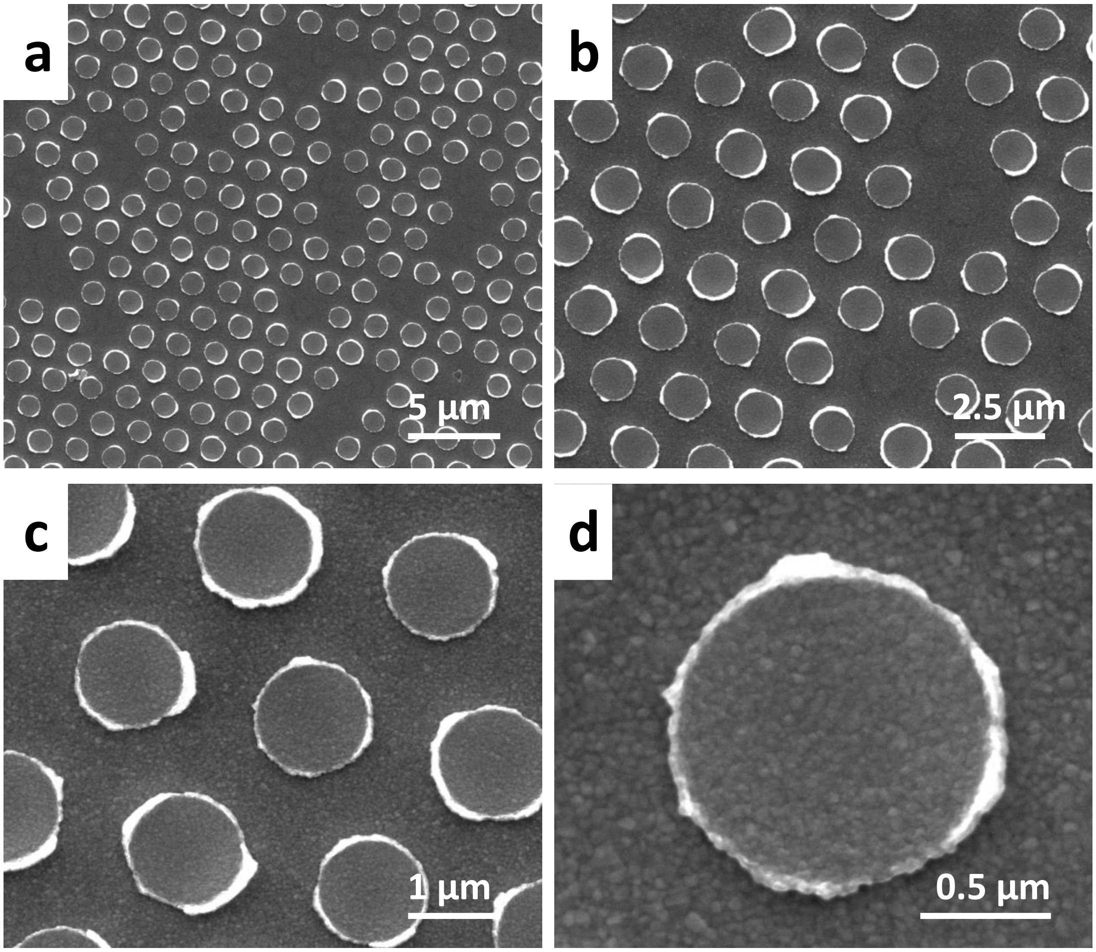

Figure S19: SEM images of Cu dots on Ag with a carbon interlayer at different degrees of magnification. Some dots are missing, most likely because the adhesion between the carbon and silver might be weak for some dots.

Supplemental electrocatalysis data for Cu dots/lines on Au and Ag

Catalysis results for 18.2% Cu on Au

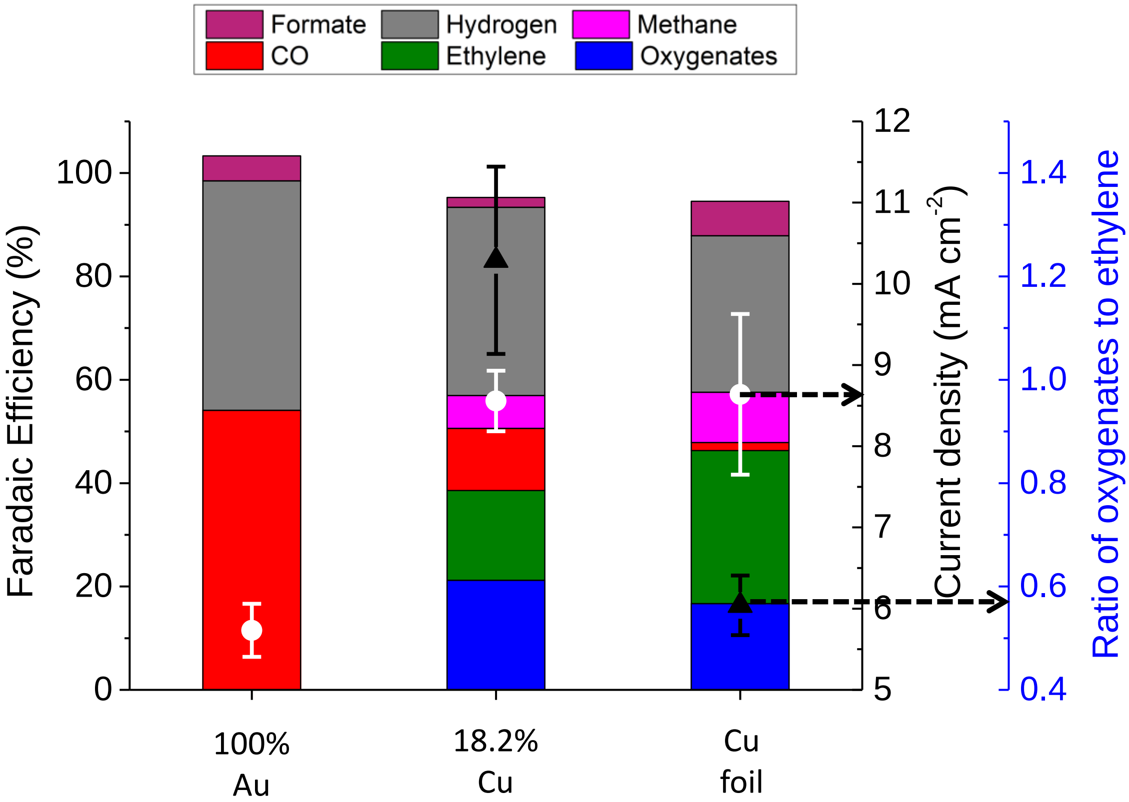

Figure S20: Faradaic efficiency and ratio of oxygenates to ethylene (in terms of faradaic efficiency) for Au substrate (100% Au) and 18.2% Cu lines on a Au substrate. Data for Cu foil is shown for reference. White circles represent the current density and black triangles represent the ratio of oxygenates to ethylene. Error bars are standard deviations for replicate experiments, typically 3.

Breakdown of oxygenates for the Cu dots/lines on Ag system (C_2 products)

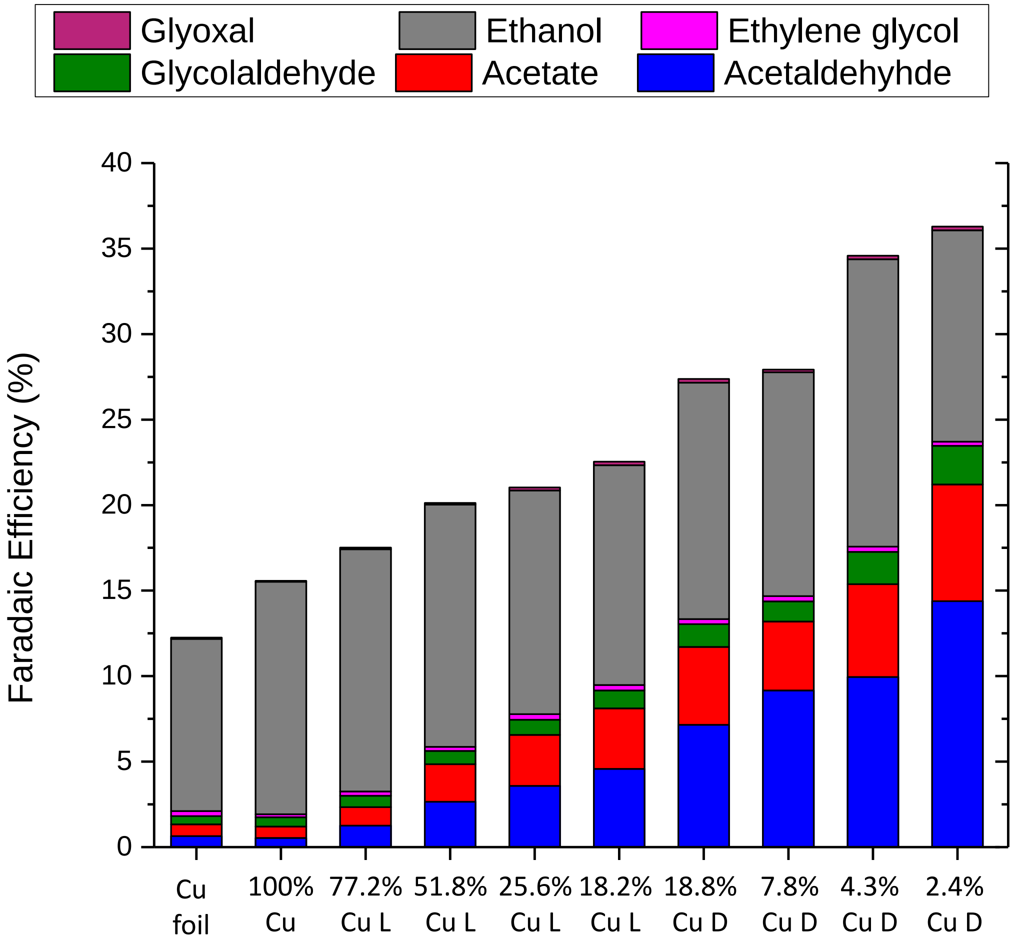

Figure S21: Faradaic efficiency to C_2 oxygenates for the Cu dots/lines on Ag substrate system. Data for Cu foil is shown for reference. L stands for lines and D stands for dots.

Breakdown of oxygenates for the Cu dots/lines on Ag system (C_3 products)

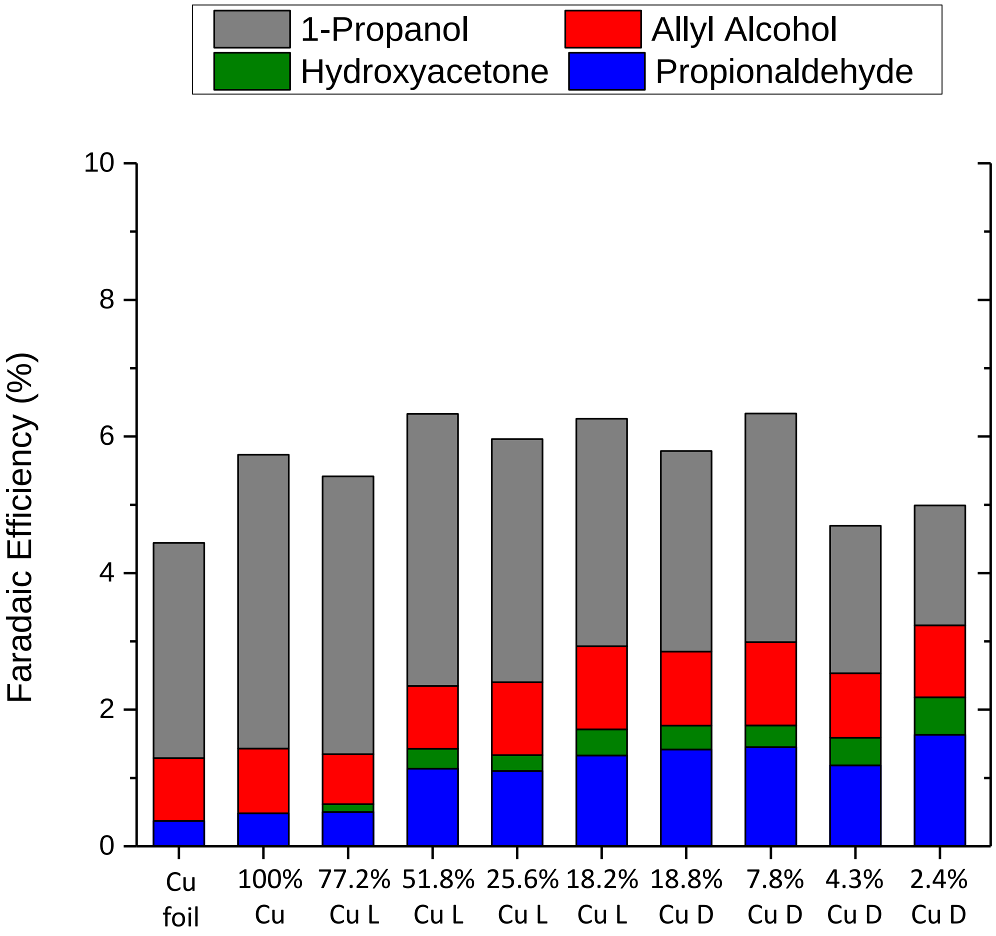

Figure S22: Faradaic efficiency to C_3 oxygenates for the Cu dots/lines on Ag substrate system. Data for Cu foil is shown for reference. L stands for lines and D stands for dots.

Control experiments and simulations

Catalysis results of Cu dots with carbon interlayer

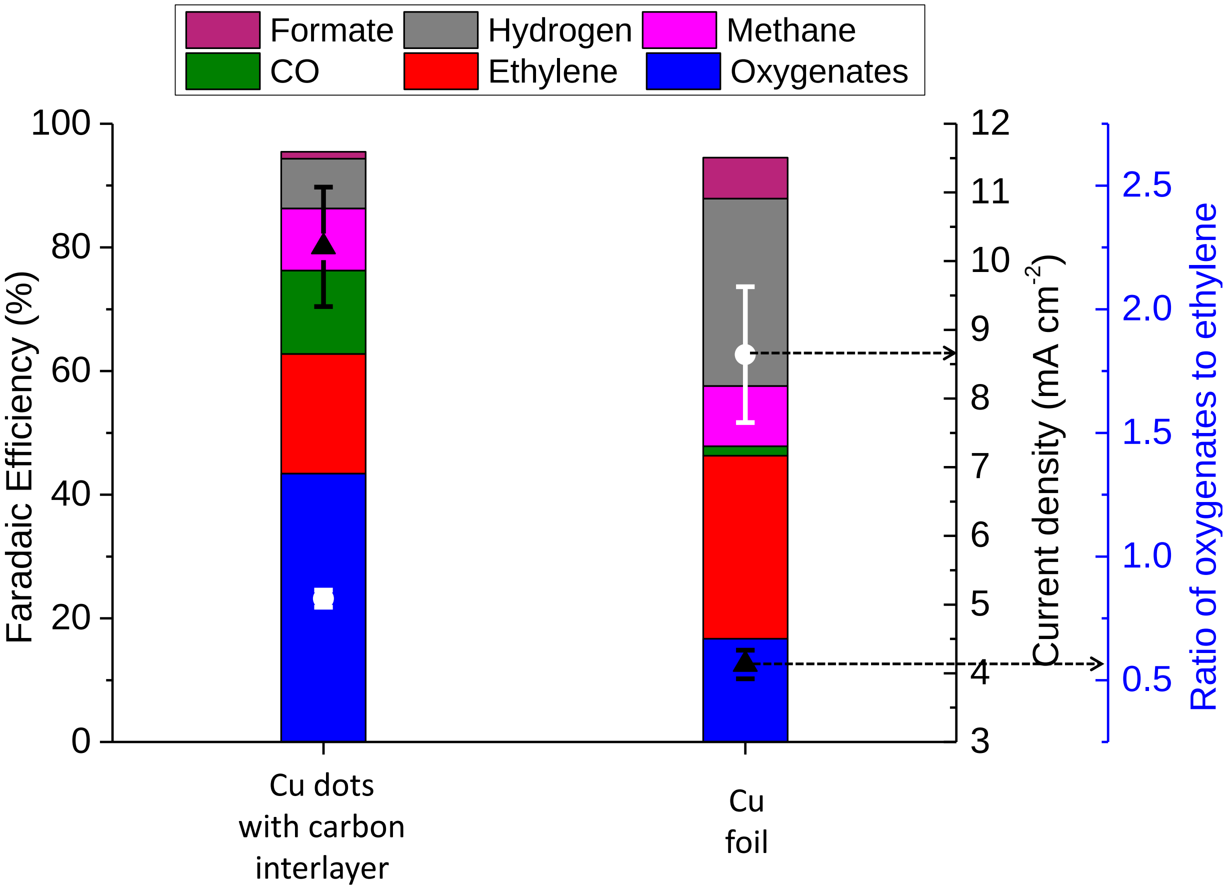

Figure S23: Faradaic efficiency and ratio of oxygenates to ethylene (in terms of faradaic efficiency) for Cu dots on Ag substrate with a carbon interlayer. Data for Cu foil is shown for reference. White circles represent the current density and black triangles represent the ratio of oxygenates to ethylene. Error bars are standard deviations for replicate experiments, typically 3.

Effects on partial current densities for 18.2% Cu dots on Ag vs Au substrate

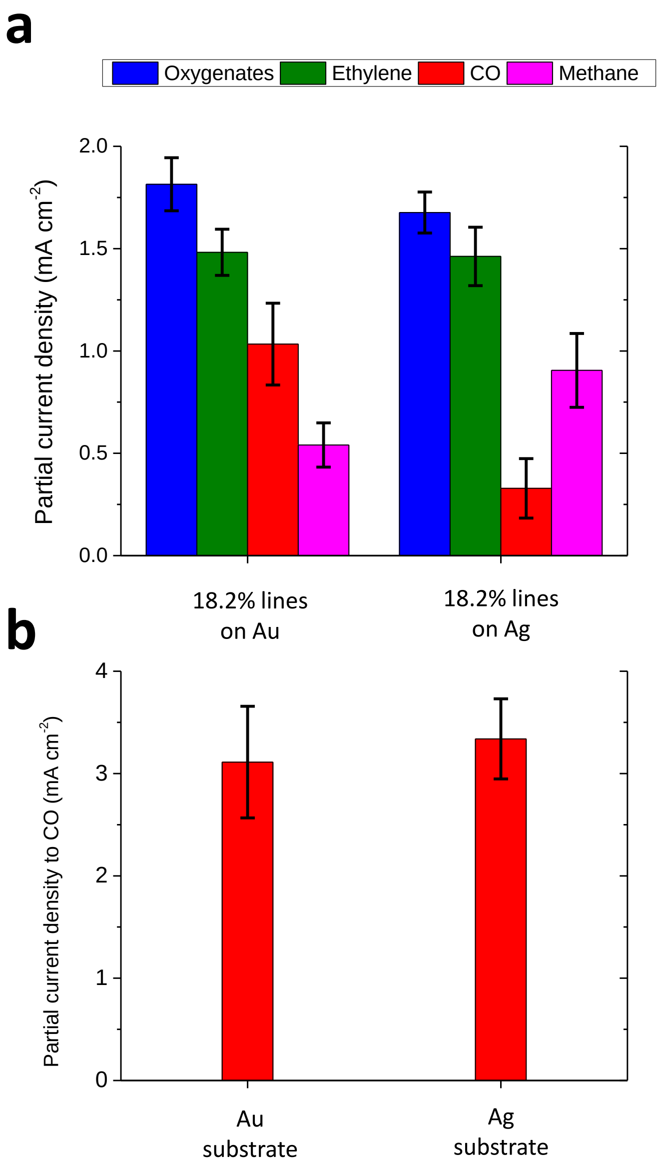

Figure S24: (a) Partial current density to oxygenates, ethylene, CO and methane for the 18.2% Cu lines on Au or Ag systems. (b) Partial current density to CO for the Au substrate and Ag substrate. The partial current density to CO for both Au and Ag substrates are very similar and this leads to very similar partial current densities to ethylene and oxygenates for the 18.2 % Cu lines on Au or Ag. In both cases, the oxygenate to ethylene ratio is very similar as well. Error bars are standard deviations for replicate experiments, typically 3.

CO reduction on Cu dots on Ag compared to Cu film

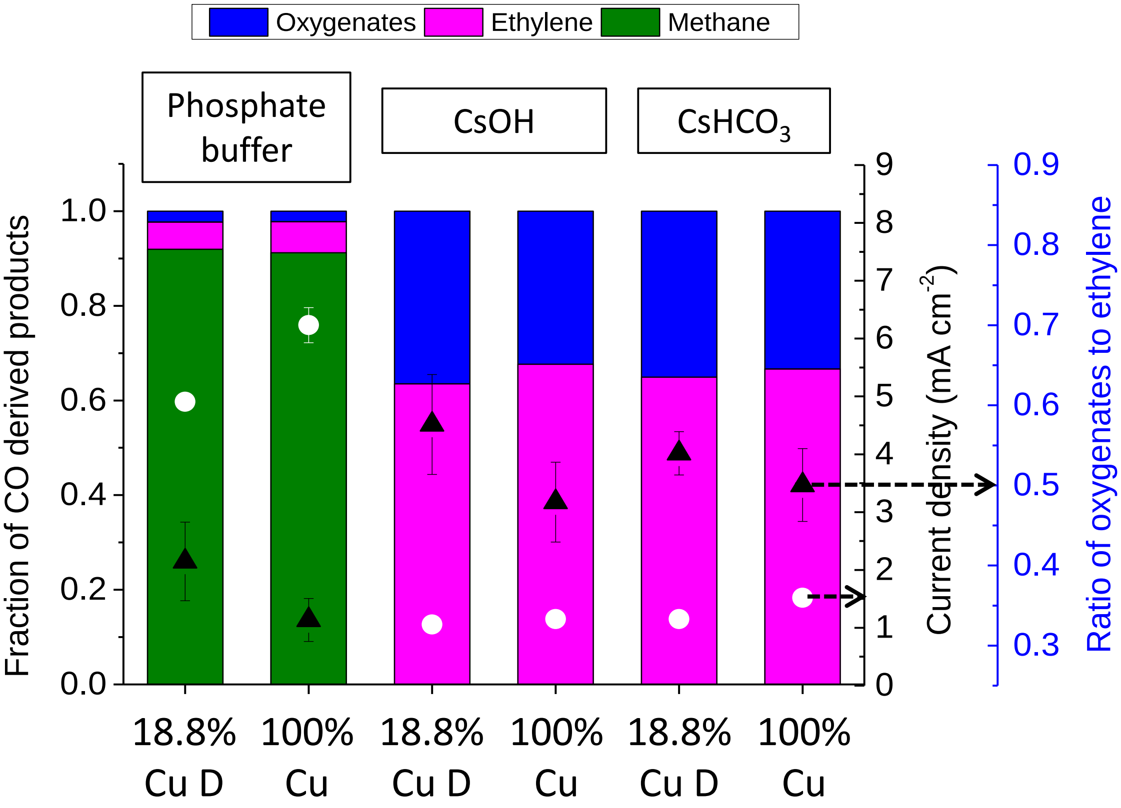

Figure S25: Fraction of CO derived products going into oxygenates, ethylene and methane (in terms of faradaic efficiency for CO reduction) under 3 different conditions with 18.8% Cu dots on Ag and 100% Cu on Ag. A potential of -1.0 V vs RHE was applied with the 0.1 M phosphate buffer (pH 7) and a potential of -0.7 V vs RHE was applied for both the 0.1 M CsOH and 0.1 M $CsHCO_3$ electrolyte. White circles represent the current density and black triangles represent the ratio of oxygenates to ethylene. In contrast with the results obtained for CO_2 reduction, there is no significant difference in the product distribution and ratio of oxygenates to ethylene for CO reduction because Ag is no longer able to generate CO for sequential catalysis. Error bars are standard deviations for replicate experiments, typically 3.

Modeling of surface pH and CO_2 concentration

To rule out the effect of pH on the product distribution of CO_2R, the surface pH and CO_2 concentration was modeled for our catalyst systems. A similar approach to our previous work was adopted in a 2D model, which includes homogenous bicarboncate/carbonate buffer reactions in the boundary layer.[1] Figure S26a shows the pH contours established during CO_2R and Figure S26b shows the pH profile along the surface for the 55% AuCu device when both Au and Cu lines are actuated.

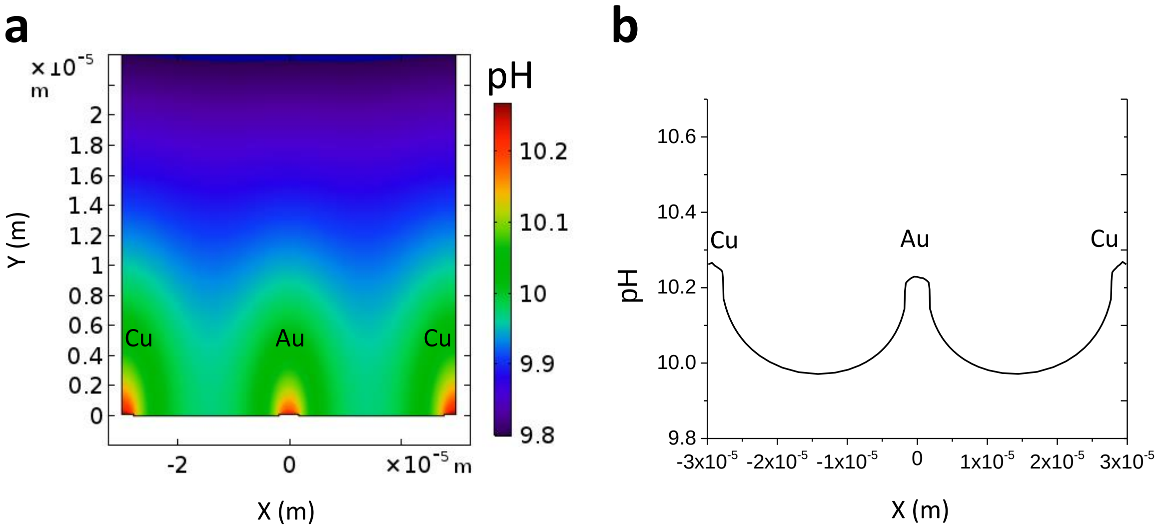

Figure S26: (a) pH contours established during CO_2R and (b) pH profile along the surface for the 55% AuCu device when both Au and Cu lines are actuated.

Table S5, S6 and S7 summarizes the surface pH and CO_2 concentration for the AuCu device systems when both Au and Cu are actuated, Cu only and Au only respectively.

Table S5: Surface pH and CO_2 concentration for the AuCu device systems when both Au and Cu are actuated.

Au + Cu (both sets of lines actuated)	Surface pH on Cu lines	Surface CO_2 concentration on Cu lines (mM)	Surface pH on Au lines	Surface CO_2 concentration on Au lines (mM)
55%	10.27	12.0	10.23	12.3
21%	10.01	14.1	10.21	12.7
11%	9.88	15.5	10.12	13.7
3%	9.59	19.6	9.89	16.9

Table S6: Surface pH and CO_2 concentration for the AuCu device systems when only Cu is actuated

Cu only	Surface pH on Cu lines	Surface CO_2 concentration on Cu lines (mM)
55%	10.22	16.4
21%	10.19	18.6
11%	9.96	23.2
3%	10.00	25.9

Table S7: Surface pH and CO_2 concentration for the AuCu device systems when only Au is actuated

Au only	Surface pH on Au lines	Surface CO_2 concentration on Au lines (mM)
55%	9.81	18.0
21%	9.78	19.1
11%	9.81	17.6
3%	9.84	15.7

As seen from the modeling results on the interdigitated devices, the surface pH of the different systems is not too drastically different as well and come within 0.7 pH units of each other.

The surface pH and CO_2 concentration for the Cu dots/lines on Ag system were also modeled and the results are shown in Table S8.

Table S8: Surface pH and CO_2 concentration for the Cu dots/lines on Ag system

Sample	Surface pH	Surface CO_2 concentration (mM)
Cu foil	10.11	12.0
100%	10.28	8.9
77.2% Cu Lines	10.07	12.9
51.8% Cu Lines	10.05	13.2
25.6% Cu Lines	9.87	16.7
18.2% Cu Lines	9.85	17.1
18.8% Cu Dots	9.95	14.9
7.8% Cu Dots	9.84	17.3
4.3% Cu Dots	9.86	16.4
2.4% Cu Dots	9.75	17.8

From the pH modeling results, because we are not in a CO_2 limited regime, the surface pH of the different catalyst systems stays within 0.5 pH units and is therefore very similar regardless of the sample. We therefore conclude that pH alone cannot account for the differences in the product distribution that is observed.

Electrochemical measurements with CO_2/CO mixtures

Here we show that our catalytic outcomes we obtained on our micropatterned catalyst systems cannot be obtained by simply flowing in mixtures of CO_2 and CO. This is because in our system, a local source of CO can be established around the Cu regions without reducing the bulk CO_2 concentration, thereby establishing a non-equilibrium state on the surface. Such a scenario would not be achievable with mixtures of CO_2 and CO as precursors.

To explain this, we first consider an experiment where a mix of CO_2 and CO is provided to the cell; the concentration of CO_2 and CO in the electrolyte would be proportional to their respective partial pressures. For example under ambient pressure, if the partial pressure of CO is x atm, the partial pressure of CO_2 is 1-x atm. This means that the concentration of CO_2 in the electrolyte would be 33.4*(1-x) mM and the concentration of CO in the electrolyte would be 1*x mM (by Henry's Law). (Note: the solubility of CO_2 and CO in H_2O is 33.4 mM and 1 mM respectively). For example, if a 7:3 (CO_2:CO) mix is used, the respective CO_2 and CO concentrations in the bulk would be 23.38 mM and 0.3 mM. Therefore, increasing the CO concentration comes at the cost of reducing the bulk CO_2 concentration, which could actually lower the CO_2 supply and reduce the CO_2 concentration on the surface. To demonstrate this, we have carried out a series of experiments performed with different mixtures of CO_2 and CO (Table S9) with Cu foil as the working electrode. Control experiments were also carried out where mixtures of CO_2 and Argon were used instead (Table S10). Besides the different gas mixtures, all experimental conditions used were identical to the CO_2R catalysis measurements reported in the main text.

Table S9: Faradaic efficiency towards H_2, C_1 and C_2/C_3 as well as ratio of oxygenates to ethylene for different mixtures of CO_2/CO. All experiments were carried out on Cu foil with identical conditions to the CO_2R catalysis measurements reported in the main text.

CO (atm)	CO concentration (mM)	CO_2 (atm)	CO_2 concentration (mM)	Faradaic Efficiency (%)			Oxygenate to ethylene ratio
				H_2	Total C_1	Total C_2/C_3	
0.1	0.1	0.9	30.1	35.5	12.6	49.3	0.62
0.2	0.2	0.8	26.7	47.6	13.5	40.8	0.63
0.3	0.3	0.7	23.4	50.7	14.5	35.6	0.64

Table S10: Faradaic efficiency towards H_2, C_1 and C_2/C_3 as well as ratio of oxygenates to ethylene for different mixtures of CO_2/Ar. All experiments were carried out on Cu foil with identical conditions to the catalysis measurements reported in the main text.

Argon (atm)	Faradaic Efficiency (%)			Oxygenate to ethylene ratio
	H_2	Total C_1	Total C_2+C_3	
0.1	48.7	15.2	31.6	0.53
0.2	54.0	15.1	24.9	0.47
0.3	57.1	15.3	22.0	0.49

As expected, adding in CO to the gas mix results in evident CO_2 depletion due to the increasing hydrogen faradaic efficiency and decreasing C_2/C_3 faradaic efficiency with higher CO partial pressure (Table S9). These trends are similar to what was observed when a mixture of CO_2/Ar was used instead (Table S10). This is probably because a high bulk CO_2 concentration is required to generate a high *CO coverage on Cu, which is essential for C-C coupling.[2,3]

For our micropatterned catalyst systems, the additional local source of CO provided does not come at the cost of reducing the bulk CO_2 concentration. This high local concentration of CO exists as a non-equilibrium state on the surface. This possibly allows for an ever higher *CO coverage than what would normally be possible under typical experimental conditions. The catalytic outcomes achievable in our systems therefore ***could not*** be elucidated by simply using CO_2 and CO as precursors in a partial pressure experiment.

Based on the CO transport modeling results (Figure 2) for the AuCu device system, it is observed that the modeled CO concentration can exceed the solubility limit of 1 mM. This is entirely possible because when a gas product is formed from an electrode, a high local supersaturation of this gas can be established. This effect is well-known and has been extensively documented in the literature.[4–8] The degree of local supersaturation is controlled by bubble nucleation and growth kinetics, which depend on the electrode surface conditions. If a surface possesses a high density of bubble nucleation sites (e.g. high roughness or crevices), bubbles nucleation occurs quickly and a lower degree of supersaturation results. However, for smooth surfaces, bubble nucleation can be suppressed and a high degree of supersaturation results. Our catalyst systems are fabricated with thin-film deposition techniques, which result in very smooth surfaces allowing for a high degree of CO supersaturation, which is available to Cu regions for further reduction. The fact that this most of this extra CO does not simply nucleate into bubbles and leave the boundary layer is evidenced by the fact that the observed CO partial current is significantly lower in the Au+Cu case compared to the Au only case (Figure 5c). Table S11 summarizes the maximum CO concentration in the boundary layer (based on the model) when both Au and Cu lines are actuated.

Table S11: Estimated maximum CO concentration (based on transport modeling) for each AuCu device system when both Au and Cu lines are actuated.

Sample	Maximum CO concentration from model (mM)
55% AuCu	0.862
21% AuCu	3.08
11% AuCu	5.41
3% AuCu	12.1

CO transport modeling was also carried out for the Cu dots/lines on Ag system as well and Table S12 shows the maximum CO concentration in boundary layer. In this case, Cu was also assumed to be an ideal sink.

Table S12: Estimated maximum CO concentration (based on transport modeling) for each catalyst in the Cu dots/lines system.

Sample	Maximum CO concentration from model (mM)
77.2% Cu Lines	0.239
51.8% Cu Lines	0.760
25.6% Cu Lines	2.52
18.2% Cu Lines	4.77
18.8% Cu Dots	0.168
7.8% Cu Dots	0.503
4.3% Cu Dots	0.962
2.4% Cu Dots	2.13

Table S12 shows that for some cases, the CO concentration does go above the solubility limit (1 mM). However, most of this CO that is generated by Ag gets further reduced by Cu regions as evidenced by the low CO faradaic efficiency observed, even at very low areal coverages of Cu (Figures 6 and 7).

CO reduction experiments at different partial pressures of CO

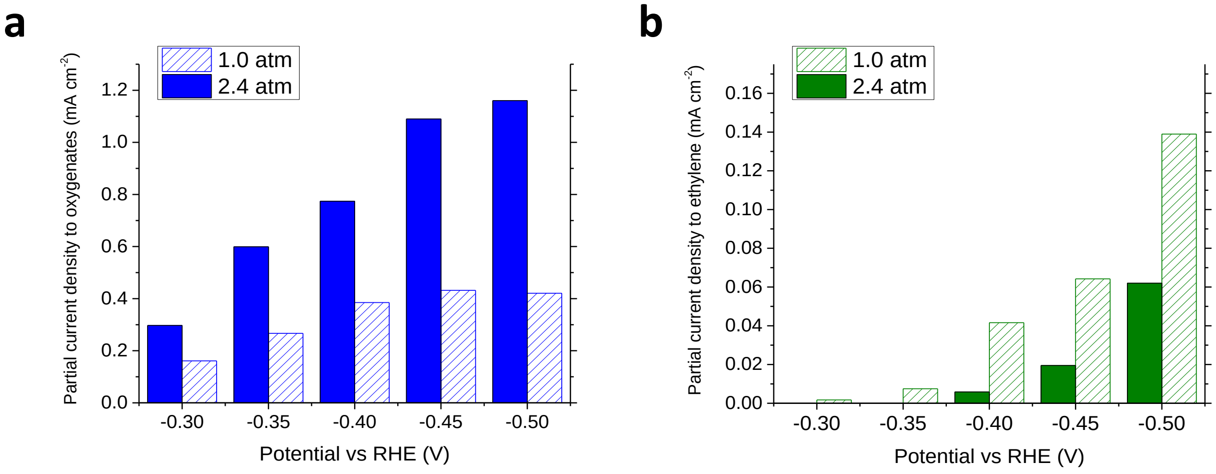

Figure S27: Partial current density data towards: (a) oxygenates and (b) ethylene for CO reduction at 1.0 atm and 2.4 atm of CO for “OD-Cu 1” as reported by Kanan and co-workers.[9] At the higher CO pressure (2.4 atm), ethylene partial current density is decreased, whereas oxygenate partial current density is increased.

Energy efficiency calculations

In this section, energy efficiency calculations for the Cu dots/lines on Ag system are shown in detail. To calculate the energy efficiency (η) the following equation is used:

$$\eta = \frac{\sum E_i^0 * FE_i}{E_{cell}} \qquad (3)$$

where E_i^0 is the standard thermodynamic potential for converting CO_2 to a product *i*, FE_i is the faradaic efficiency for product *i* and E_{cell} is the total cell voltage (without any IR compensation).

In this work, only three electrode measurements were carried out and as such, the E_{cell} value in each case must be calculated. Also, a Pt foil electrode was used as the counter electrode, which requires a high overpotential. However, in an optimal system, a catalyst which has high activity for oxygen evolution should be used instead. Thus, we will calculate E_{cell} values assuming that an IrO_2 catalyst (described in our previous work[10]) was used instead. Based on data from previous work, we calculated the combined solution and membrane resistance to be a value of 197 Ω, with 0.1 M $CsHCO_3$ used as the electrolyte.

Therefore, E_{cell} is calculated by the following equation:

$$E_{cell} = V_{anode} - V_{cathode} + IR \qquad (4)$$

where V_{anode} is the potential of the anode (with IR compensation), $V_{cathode}$ is the potential of the cathode (with IR compensation), I is the total current flowing through the electrochemical cell and R is the combined solution and membrane resistance (197 Ω).

Table S13 shows the calculated E_{cell} values for each case.

Table S13. Values used to calculate E_{cell} for each catalyst system

Catalyst system	V_{anode}* (V vs RHE)	$V_{cathode}$ (V vs RHE)	I (mA cm^{-2})	Estimated E_{cell} (V)
Cu foil	1.59	-1.0	8.67	4.29
100 % Cu	1.63		10.6	4.64
77.2 % Cu lines	1.57		8.02	4.15
51.8 % Cu lines	1.57		7.86	4.11
25.6 % Cu lines	1.49		6.00	3.67
18.2 % Cu lines	1.48		5.75	3.63
18.8 % Cu dots	1.53		6.72	3.85
7.8 % Cu dots	1.48		5.83	3.64
4.3 % Cu dots	1.49		5.91	3.66
2.4 % Cu dots	1.44		4.86	3.40

*Calculated based on data from previous work with an IrO_2 catalyst.[10]

E_i^0 values for each product are also listed in our previous work[10] and is used to calculate energy efficiency based on equation (3). Table S14 lists the calculated energy efficiency values for each catalyst system.

Table S14. Total energy efficiency, C_2/C_3 product energy efficiency, C_1 product energy efficiency and hydrogen energy efficiency for each catalyst system.

Catalyst system	η_{total}	$\eta_{C2/C3}$	η_{C1}	$\eta_{Hydrogen}$
Cu foil	26.18%	12.47%	5.04%	8.68%
100 % Cu	24.23%	14.26%	3.81%	6.16%
77.2 % Cu lines	26.71%	15.45%	4.98%	6.28%
51.8 % Cu lines	26.98%	15.61%	5.03%	6.35%
25.6 % Cu lines	30.62%	16.44%	7.26%	6.93%
18.2 % Cu lines	30.39%	17.49%	7.46%	5.44%
18.8 % Cu dots	29.22%	18.34%	7.21%	3.67%
7.8 % Cu dots	30.87%	19.14%	6.54%	5.19%
4.3 % Cu dots	30.95%	21.41%	7.16%	2.38%
2.4 % Cu dots	34.68%	20.73%	12.09%	1.86%

Additionally, for each catalyst system, the energy consumed per mol of C_2/C_3 products generated can be calculated as well. These values are summarized in Table S15.

Table S15. Calculations to determine the energy consumed per mole of C_2/C_3 product generated

Catalyst system	Cell power (W)	Power consumed to generate C_2/C_3 products (W)	Energy consumed per mole of C_2/C_3 product generated (J mol^{-1})
Cu foil	0.0371	0.0172	5029
100 % Cu	0.0471	0.0270	5461
77.2 % Cu lines	0.0332	0.0183	4781
51.8 % Cu lines	0.0322	0.0177	4734
25.6 % Cu lines	0.0220	0.0113	4157
18.2 % Cu lines	0.0211	0.0114	4073
18.8 % Cu dots	0.0258	0.0154	4243
7.8 % Cu dots	0.0214	0.0126	4021
4.3 % Cu dots	0.0218	0.0144	3965
2.4 % Cu dots	0.0166	0.00973	3552

It is noted that even though the systems with lower Cu coverages appear to be more energy efficient and require less energy to generate C_2/C_3 products, it comes at the cost of a lower partial current to these products.

Supplemental References

1 Y. Lum, B. Yue, P. Lobaccaro, A. T. Bell and J. W. Ager, *J. Phys. Chem. C*, 2017, **121**, 14191–14203.

2 R. B. Sandberg, J. H. Montoya, K. Chan and J. K. Nørskov, *Surf. Sci.*, 2016, **654**, 56–62.

3 Y. Huang, A. D. Handoko, P. Hirunsit and B. S. Yeo, *ACS Catal.*, 2017, **7**, 1749–1756.

4 G. Sakuma, Y. Fukunaka and H. Matsushima, *Int. J. Hydrogen Energy*, 2014, **39**, 7638–7645.

5 S. Jones, *Adv. Colloid Interface Sci.*, 1999, **80**, 27–50.

6 D. Fernández, P. Maurer, M. Martine, J. M. D. Coey and M. E. Möbius, *Langmuir*, 2014, **30**, 13065–13074.

7 T. Kadyk, D. Bruce and M. Eikerling, *Sci. Rep.*, 2016, **6**, 38780.

8 C. Brussieux, P. Viers, H. Roustan and M. Rakib, *Electrochim. Acta*, 2011, **56**, 7194–7201.

9 C. W. Li, J. Ciston and M. W. Kanan, *Nature*, 2014, **508**, 504–507.

10 G. Gurudayal, J. Bullock, D. F. Sranko, C. M. Towle, Y. Lum, M. Hettick, M. C. Scott, A. Javey and J. W. Ager III, *Energy Environ. Sci.*, 2017.